catalysts

MDPI

Article

Effect of Decoration of C@TiO_2 Core-Shell Composites with Nano-Ag Particles on Photocatalytic Activity in 4-Nitrophenol Degradation

Karol Sidor, Róża Lehmann, Anna Rokicińska, Tomasz Berniak, Marek Dębosz and Piotr Kuśtrowski *

Faculty of Chemistry, Jagiellonian University, Gronostajowa 2, 30-387 Kraków, Poland
* Correspondence: piotr.kustrowski@uj.edu.pl; Tel.: +48-12-686-2415

Abstract: Photoactive TiO_2 materials based on a C@TiO_2 core-shell structure synthesized according to the bottom-up strategy using a spherical resin core were presented in relation to commercial TiO_2 (P25) used as a reference material. The studied TiO_2 materials were modified with Ag nanoparticles using two alternative methods: impregnation and precipitation. Depending on the deposition technique used, different distributions of the Ag modifier were achieved within the TiO_2 structure. As confirmed by X-ray diffraction (XRD) and scanning electron microscopy (SEM) measurements, the precipitation technique resulted in the formation of almost twice smaller, highly dispersed Ag nanoparticles compared to impregnation. Furthermore, the effect of the performed modification on the textural properties (low-temperature N_2 adsorption) and surface composition (X-ray photoelectron spectroscopy) was determined. The phase composition of the TiO_2 support as well as the dispersion of the Ag modifier significantly affected the energy gap determined from UV–Vis spectra and, consequently, their performance in the process photodegradation of 4-nitrophenol tested as a model molecule. In the case of the @TiO_2 material modified with highly dispersed Ag, significantly higher photoactivity in the visible light range was observed than in the presence of analogous P25-based materials.

Keywords: core-shell structures; TiO_2; Ag nanoparticles; photocatalysis; removal of phenolic compounds

check for updates

Citation: Sidor, K.; Lehmann, R.; Rokicińska, A.; Berniak, T.; Dębosz, M.; Kuśtrowski, P. Effect of Decoration of C@TiO_2 Core-Shell Composites with Nano-Ag Particles on Photocatalytic Activity in 4-Nitrophenol Degradation. *Catalysts* **2023**, *13*, 764. https://doi.org/10.3390/catal13040764

Academic Editor: Giusy Lofrano

Received: 31 March 2023
Revised: 9 April 2023
Accepted: 14 April 2023
Published: 17 April 2023

1. Introduction

The widespread use of organic compounds in various everyday products, such as dyes, pharmaceuticals, surfactants, pesticides or body care products, causes their release and accumulation in surface water and groundwater [1,2]. A particularly important group of harmful organic substances found in the water systems are phenol and its derivatives, which United States Environmental Protection Agency (USEPA) and European Commission classify as priority pollutants. Due to their tendency to bioaccumulation [3,4], phenolic compounds have been recognized as substances causing short- and long-term effects in animal [5] and human bodies [6]. Sources of phenolic pollutants can be divided into natural (mainly processes of decomposition of organic matter [7]) and anthropogenic, which include chemical industry, textile industry, and construction industry, as well as agriculture [8–10].

Phenol used on a large scale in industry [11] as a compound that is well soluble in water, oils, and most organic solvents (e.g., alcohols, ethers) is particularly dangerous. It is quickly and easily absorbed in human tissues through contact with skin, during breathing or ingestion, causing an allergic reaction. The above-mentioned factors and poor biodegradability have resulted in intensive development of various techniques for removing phenol from aqueous media [12]. Among them, it is possible to distinguish membrane [13] or biological methods [14]. Unfortunately, membranes are easily clogged by deposition of colloids and larger particles [12]. Furthermore, the use of microorganisms requires high

operation costs [8]. One of the key technologies for water purification is adsorption, usually carried out on activated carbons [15]. However, the systems based on the adsorption process are less effective for removing low-concentration pollutants [16]. Among other destructive methods, non-catalytic and catalytic wet (air) oxidation of phenolic compounds should be mentioned [17]. In the latter case, homo- (mainly transition metal ions) and heterogeneous systems (transition metal oxides (CuO, NiO, Co_3O_4, Fe_2O_3, MnO_x), mixed oxides (CeO_2-ZrO_2, CeO_2-TiO_2) or noble metals (Ru, Rh, Rd, Pt) deposited on supports) are used [17–20]. The main disadvantage of the methods based on wet oxidation is the use of special reaction chambers, which are required due to the process conditions—elevated temperature and pressure.

Photocatalytic oxidation of phenolic compounds is a destructive method devoid of high temperatures and pressures. According to the band theory, an energy quantum (photon) results in the electron transfer from valence to conduction band of a photocatalyst. The generated electron hole in contact with a water molecule can form a hydroxyl radical. Similarly, in the case of an excited electron in the conduction band, contact with an oxygen molecule can lead to the formation of superoxide anion radical [21]. The degradation of organic pollutants occurs through the attack of the reactive oxygen species generated on the surface of photocatalyst. In the model reaction of photocatalytic oxidation, full mineralization of phenolic impurities occurs [22]. A great benefit of environmentally friendly photocatalytic methods is the possibility of multiple uses of a photocatalyst [16,23].

Examples of photoactive materials studied in the photodegradation of phenolic pollutants include ZnO [24], CdS [25], SnO_2 [26], WO_3, g-C_3N_4 [27], and Bi_2SiO_5 [28]. However, one of the most commonly used semiconductor materials for the photocatalytic applications is highly efficient and inexpensive TiO_2 [26,29]. The effect of TiO_2 modification on its photoactivity has been widely examined. It was revealed that the degradation rate can be enhanced by facilitating adsorption of pollutants on the surface of photocatalyst. Such promoting effect in phenol removal was observed e.g., after depositing Fe_2O_3 on commercial TiO_2 (Degussa P25) [30]. The phase composition of P25 (ca. 80% anatase and 20% rutile) causes the band gap, i.e., the photon energy window necessary for excitation, to be 3.2 eV, which determines its use in the UV range (290–380 nm) [31]. Nevertheless, it is possible to introduce an additional phase into the semiconductor structure, which allows one to modify the band gap of the obtained material in such a way as to transfer its photoactivity to the visible region [32]. An example of such an approach may be subsidizing TiO_2 with carbon, which was introduced during TiO_2 precursor precipitation using carboxylic acids (citric or ascorbic) [33]. Another non-metal used is nitrogen, which can be introduced by hydrothermal treatment of TiO_2 with TEA, urea [34] or through chemical vapor deposition (CVD) [35]. Shifting the working range of TiO_2 during the photooxidation of phenol is also obtained by doping with metals. The most commonly used for this purpose are V, Cr [36], Mo, Co, Cu [37], Au, Ru [38], Ag, or Pd [39]. The application of metals, including Ag, allows to increase the photocatalytic efficiency of the material by influencing the previously mentioned TiO_2 band gap and trapping excited electrons [39]. 5% wt. Ag(0) supported on TiO_2 nanorods exhibited an enhanced efficiency in the phenol photodegradation especially when sunlight was used [40]. Furthermore, commercial anatase subsidized by 1% wt. Ag showed an improved photoactivity compared to pure anatase also in the case of using the UV radiation [41].

Although TiO_2 is generally considered to be a non-toxic substance [29], recent studies have shown that the use of TiO_2 with nano-sized grains can have a negative impact. The genotoxicity of nano-TiO_2 cannot be ruled out [42], and its presence in plant and animal organisms leads to increased oxidative stress [43]. Therefore, when looking for optimal forms of photoactive nano-TiO_2, one should focus on systems that are relatively easy to isolate from the environment after the operation procedure. In this work, attention is paid to spherical C@TiO_2/Ag core-shell materials. In their case, nano-TiO_2 is deposited on a carbon core obtained by carbonization of spherical resin template with a particle size of

ca. 600 nm. It is shown that decorating the TiO_2 photocatalyst with Ag modifier allows to increase significantly its activity in the visible light range.

2. Results

In this work, (i) oxide shells from synthesized C@TiO_2 core-shell structures and (ii) commercial P25 were used as photoactive TiO_2 materials. The synthesis of the C@TiO_2 material started with the formation of spherical resin (RFM), which in the next step was a scaffold for the deposition of the TiO_2 precursor, and finally, the obtained material was subjected to the carbonization process. Figure 1 comparatively shows particle size distribution determined by the dynamic light scattering technique in water suspension for P25, RFM core and corresponding C@TiO_2 structure.

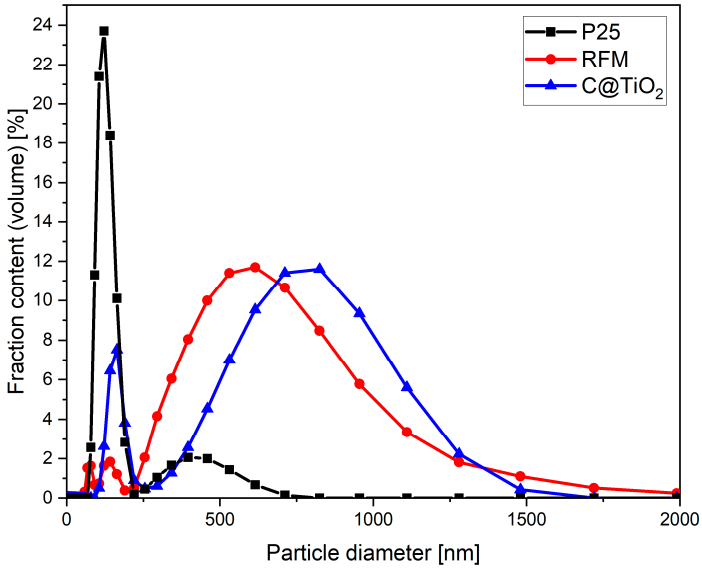

Figure 1. DLS measurements of particle size dispersion of commercial P25, RFM template, and C@TiO_2.

It is clear that the advantage of using a resin template is to increase the particle size of the TiO_2-containing material and to improve dispersion of the photoactive component. The P25 photocatalyst contains mainly grains with diameters close to 120 nm, which are formed by combining individual TiO_2 crystallites [44]. In the case of the synthesized C@TiO_2 material, the TiO_2 precursor is deposited on a template with grain diameters of ca. 600 nm. As a result of deposition and carbonization, the grain size of the created composite increases to ca. 780 nm. Considering that RFM shows a tendency to shrink at elevated temperatures [45], it should be assumed that the thickness of the produced TiO_2 shell calculated by a simple difference in relation to the size of RFM grains, amounting to 90 nm, is probably underestimated. On the other hand, it should be however kept in mind that the DLS method determines hydrodynamic radii, which overestimate the size of the observed particles—in particular, those of irregular shapes.

The Ag phase was introduced as a modifier into the TiO_2-containing materials using two different methods—impregnation (IMP) and precipitation (H_2O). It was expected to achieve its different distribution, in particular resulting from the depth of penetration during the performed modification of the C@TiO_2 composite. In the case of the IMP method, the Ag phase should be deposited more superficially, without thorough penetration of the composite pores. On the other hand, in the first step of the precipitation procedure (H_2O method), Ag^+ ions are introduced together with the aqueous phase into the entire pore volume of the material.

In order to verify the effect of Ag deposition in the core-shell material on thermal stability of the resulting materials, thermogravimetric analysis was done (Figure 2). As

assumed, an increase in the content of the non-carbon part of the composite was observed as the result of Ag deposition. The remaining 45.75%, 46.40%, and 46.84% of the initial mass for the C@TiO_2, C@TiO_2/Ag_IMP and C@TiO_2/Ag_H_2O samples, respectively, suggest the introduction of 0.7–1.1 wt % of Ag in relation to the entire mass of the composite. Furthermore, the recorded TGA and DTA curves reveal the existence of differences in the depth of penetration of the TiO_2 shell by the metallic phase. It is worth noting that, regardless of the method used, the introduction of Ag into the structure of the core-shell material caused a shift in the oxidation of the carbon core to lower temperatures. This effect is particularly visible for the DTA curves evidencing the release of large amounts of heat during the exothermic combustion of the resol-derived carbon core [45]. The maximum of the DTA peak observed for the unmodified composite at 588 °C, for the C@TiO_2/Ag_IMP material is found at 569 °C. The presence of the TiO_2 layer on the carbon core results in faster delivery of the oxidant due to the facilitated adsorption of oxygen on its surface [46]. The introduction of the Ag phase onto the surface of the photocatalyst increases the availability of oxygen needed for the combustion of the carbon core and its activation at elevated temperatures [47]. In the case of C@TiO_2/Ag_H_2O, two peaks attributed to the combustion of the carbon part are detected. The maximum at 495 °C is associated with the Ag phase, which is deposited in the TiO_2 pores in close contact with the core of the composite. The content of this form is much higher than in the case of the C@TiO_2/Ag_IMP sample, hence such a significant shift of the combustion process towards lower temperatures. On the other hand, the carbon combustion occurring below 400 °C should be attributed to Ag deposited directly on the surface of the core.

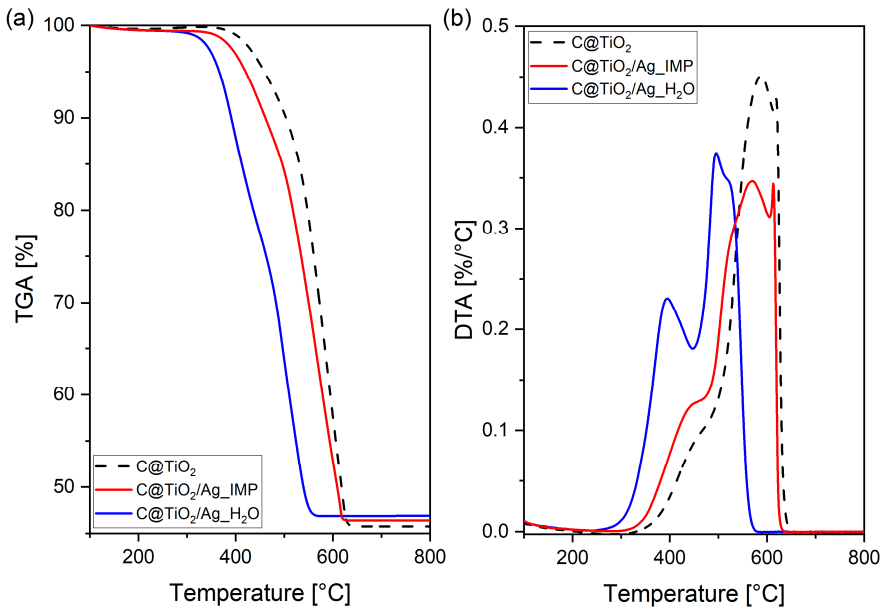

Figure 2. TGA (**a**) and DTA (**b**) analyses of the C@TiO_2 composite at oxidizing atmosphere before and after deposition of Ag using two different methods—IMP and H_2O.

Powder X-ray diffraction was used to identify the type of Ag phase deposited on C@TiO_2. As shown in Figure 3a, both Ag deposition methods allowed to form the cubic phase Ag^0, confirmed by the diffraction peaks marked with gray dashed lines at 38.2°, 44.3°, 64.4°, and 77.4°, corresponding to (111), (200), (220), and (311) planes, respectively [48]. In the case of the C@TiO_2/Ag_IMP sample, these reflections are more intense. Using the Scherrer equation (calculations for (002) peak assuming a value of K constant = 0.9) showed the average size of Ag^0 crystallites—12.4 Å (C@TiO_2/Ag_H_2O) and 23.9 Å (C@TiO_2/Ag_IMP). Thus, the application of the H_2O method resulted in obtaining a material with a higher Ag dispersion on the surface of the composite. This observation confirms the conclusions previously formulated on the basis of the TGA results. The comparative analysis for the

P25-based materials (Figure 3b) also indicates the presence of four reflections related to the presence of Ag^0. As for the C@TiO_2 materials, in the case of P25 after IMP modification, diffraction peaks of greater intensity are observed. This is reflected in the size of the Ag crystallites determined on the basis of (002) reflection (K = 0.9)—13.4 Å (P25/Ag_H_2O) and 24.3 Å (P25/Ag_IMP).

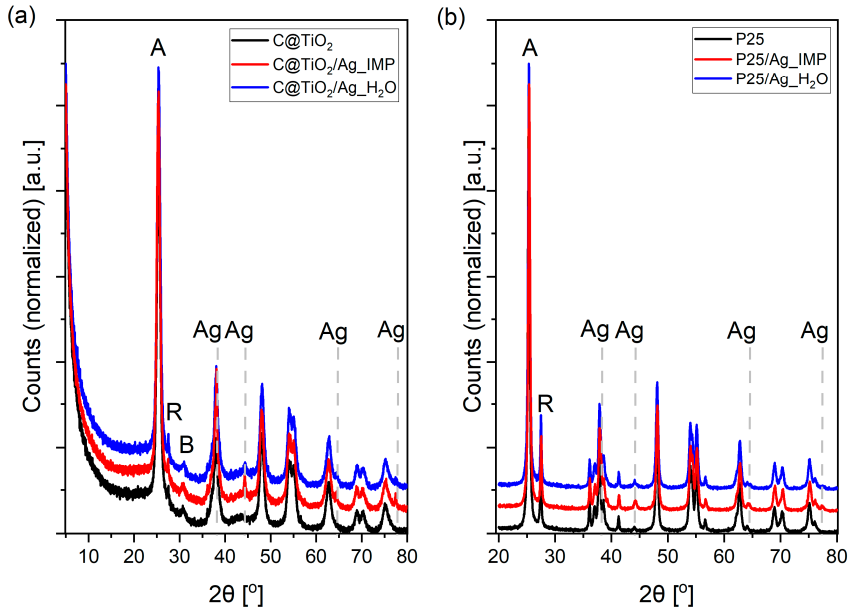

Figure 3. XRD patterns of C@TiO_2 (**a**) and P25 (**b**) materials before and after deposition of Ag using two different methods—IMP and H_2O (A—anatase, R—rutile, B—brookite).

It should be noted that the selected supports differ in the phase composition of TiO_2. Commercial P25 consists of two TiO_2 phases—anatase and rutile. In the case of C@TiO_2, the photocatalytic phase is mainly based on anatase with only small admixture of rutile and brookite. The appearance of the rutile phase, mostly manifested by the (110) reflection at 27.5°, is related to the thermal treatment at 550 °C. The reduction of the anatase → rutile phase transition temperature in the presence of Ag below 700 °C was previously reported [49]. It is also worth noting that within the broaden range of XRD patterns to lower 2θ angles for the C@TiO_2 materials, the presence of (002) and (100) diffraction maxima typical of graphite-like domains at ca. 22° and 44°, respectively, is found as a baseline raise [50].

Furthermore, the porosity of the discussed materials was studied by low-temperature nitrogen adsorption. The collected adsorption isotherms presented in Figure 4 clearly reveal a different type of porosity characterizing the materials based on C@TiO_2 and P25. In the former case, the presence of a microporous carbon core surrounded by a mesoporous TiO_2 shell is evidenced by a rapid increase in the amount of adsorbed N_2 at low relative pressures (p/p_0) and further adsorption at higher p/p_0, resulting in a mixed type of isotherm between I (characteristic of microporous solids) and IV (mesoporous solids) according to the IUPAC classification. The mesoporous nature of the shell is also confirmed by the isotherms recorded for @TiO_2 after removal of the carbon core (Figure 4b). In addition, it should be noted that the @TiO_2 oxide materials have improved porosity compared to P25 (Figure 4c). These features very well highlight the textural parameters determined with the appropriate models (Table 1).

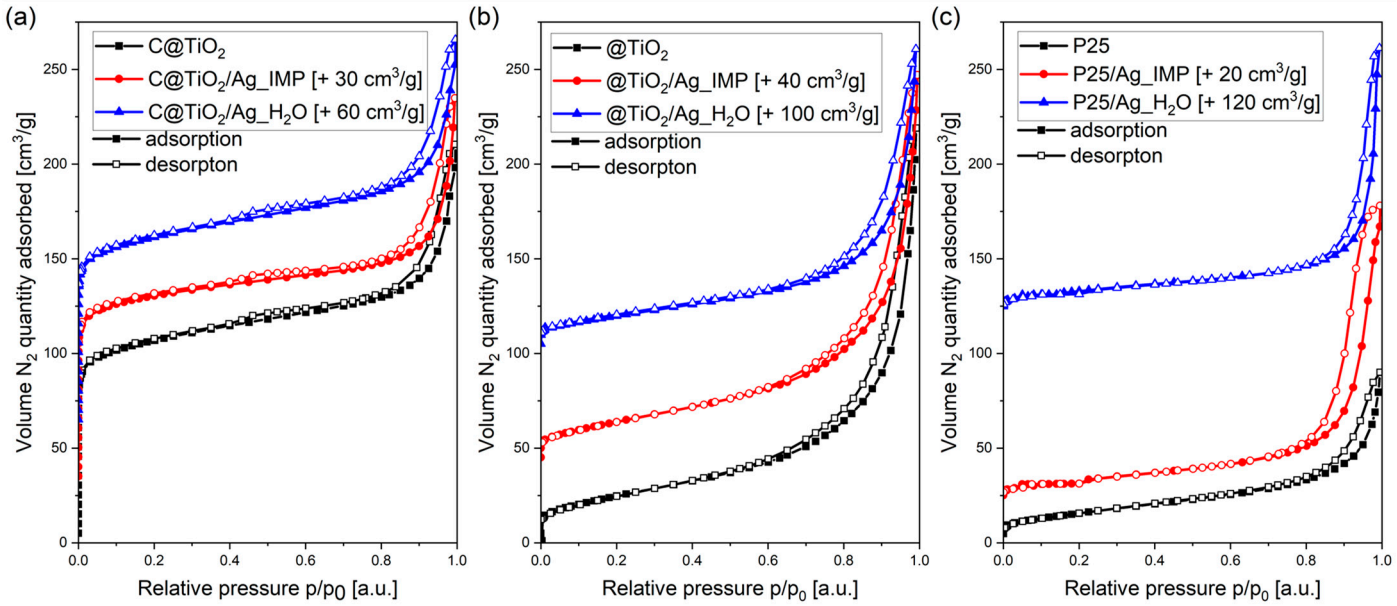

Figure 4. N_2 adsorption-desorption isotherms for C@TiO_2 (**a**), @TiO_2 (**b**) and P25 (**c**) materials before and after deposition of Ag using two different methods—IMP and H_2O.

Table 1. Textural parameters of C@TiO_2 (a), @TiO_2 (b) and P25 (c) materials before and after deposition of Ag using two different methods—IMP and H_2O.

Sample	Surface Area		Pore Volume		
	BET [$m^2 \cdot g^{-1}$]	Langmuir [$m^2 \cdot g^{-1}$]	V_{total} [a] [$cm^3 \cdot g^{-1}$]	V_{meso} [b] [$cm^3 \cdot g^{-1}$]	V_{micro} [c] [$cm^3 \cdot g^{-1}$]
C@TiO_2	404	496	0.325	0.104	0.124
C@TiO_2/Ag_IMP	375	462	0.317	0.094	0.123
C@TiO_2/Ag_H_2O	380	473	0.318	0.108	0.114
@TiO_2	91	142	0.339	0.212	0.000
@TiO_2/Ag_IMP	85	138	0.320	0.191	0.000
@TiO_2/Ag_H_2O	72	112	0.249	0.156	0.000
P25	57	89	0.139	0.080	0.003
P25/Ag_IMP	47	74	0.244	0.156	0.001
P25/Ag_H_2O	47	72	0.218	0.095	0.003

[a] single point (at $p/p_0 \sim 0.99$); [b] BJH (based on adsorption branch of isotherm); [c] t-plot.

The C@TiO_2 support exhibits the highest surface area determined by both BET (404 m^2/g) and Langmuir model (496 m^2/g). These two methods were used, taking into account the micro-mesoporous nature of the material, for which the assumptions of the BET theory are not fully met [45]. This material has comparable volumes of micro- (0.124 cm^3/g) and mesopores (0.104 cm^3/g) corresponding to similar contents of the microporous carbon core and the mesoporous oxide shell. After the Ag deposition on the composite system, a slight degradation of porosity is observed. Only the analysis of textural parameters for the systems devoid of the carbon part highlights the effect of the Ag introduction on the C@TiO_2 composite. The impregnation method causes a smaller decrease in porosity compared to the H_2O method. It should also be noted that the @TiO_2 material shows a much larger mesopore volume and, consequently, surface area. Quite interesting observations can be made by the analysis of pore volume changes after the Ag deposition on P25. There is a clear increase in the total pore volume, attributed mainly to the appearance of inter-grain porosity, which is confirmed by the jump in the amount of N_2 adsorbed at $p/p_0 \rightarrow 1.0$.

In order to better understand the properties of the photoactive oxide shell, further attention was paid to the materials with removed carbon core (@TiO_2 and P25 for comparison). The distribution of Ag on the surface of TiO_2-based materials was determined by SEM imaging together with elemental mapping (EDX) (Figure 5).

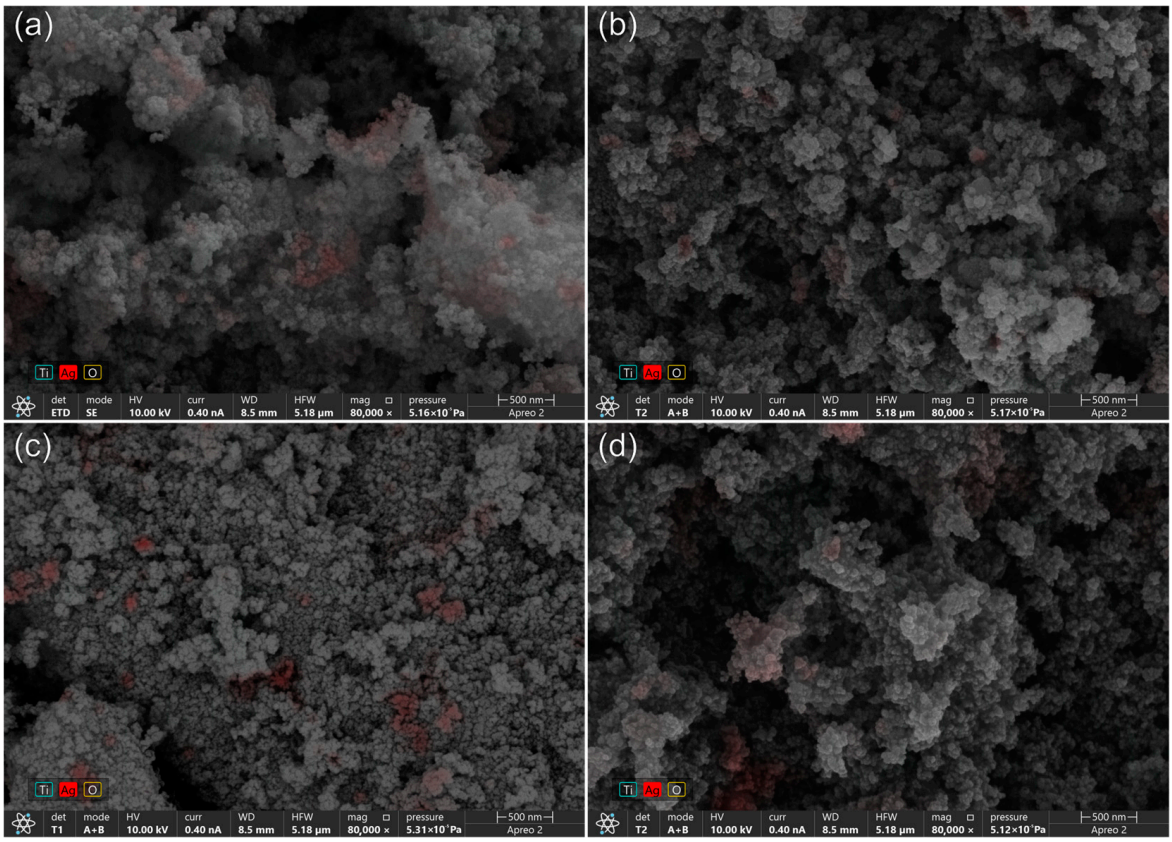

Figure 5. SEM images with EDX mapping of deposited Ag on @TiO_2/Ag_IMP (**a**), @TiO_2/Ag_H_2O (**b**), P25/Ag_IMP (**c**), and P25/Ag_H_2O (**d**).

First of all, it should be noted that the combustion of the carbon core causes the collapse of the composite structure. Spheres with diameters of several hundred nm, typical of C@TiO_2, were replaced by much smaller TiO_2 particles, which originally surrounded the core in the form of cauliflower-like structures. Generally, a similar morphology was achieved for @TiO_2 and P25. The SEM images also reveal that the IMP method results in the formation of larger Ag agglomerates than in the case of the H_2O route.

The nature and composition of the surface of @TiO_2- and P25-based materials were studied by XPS. Figure 6a–c show the core level XPS spectra of Ti 2p, O 1s and Ag 3d. The doublet of XPS Ti $2p_{3/2}$ and $2p_{1/2}$ peaks with a separation of 5.7 eV is characteristic of Ti^{4+} ions present in the TiO_2 crystal lattice [51]. No peak asymmetry is observed that would indicate the co-presence of appreciable amounts of Ti^{3+}. However, the apparent shift of the peaks towards lower binding energies after the introduction of Ag by the H_2O method should be noted (Figure 6a). The Ti $2p_{3/2}$ and $2p_{1/2}$ peaks, which for the non-modified supports and after Ag deposition using the IMP method are at 458.9–459.0 eV and 464.4–464.7 eV, change their positions to 458.4–458.5 eV and 464.0–464.2 eV, respectively (Table 2). This effect may be related to Ti^{3+} defects based on lattice distortion in TiO_2 caused by interaction with Ag [52]. Interestingly, XPS O 1s peaks also shift to lower E_b values for @TiO_2/Ag_H_2O and P25/Ag_H_2O (Figure 6b). Nevertheless, the introduction of Ag, regardless of the method, affects the shape of the XPS O 1s peaks. Lowered symmetry and tailing towards higher E_b values additionally confirms the formation of structural defects within the TiO_2 lattice [53]. It should be noted that the peak positions characteristic of

lattice oxygen O^{2-} from the TiO_2 and Ag_2O crystal lattices were previously reported at 530.5–531.2 eV and 528.9–530.1 eV, respectively [54]. No peak corresponding to chemisorbed O_2 molecules (at E_b > 533 eV) is observed for any of the tested materials [55].

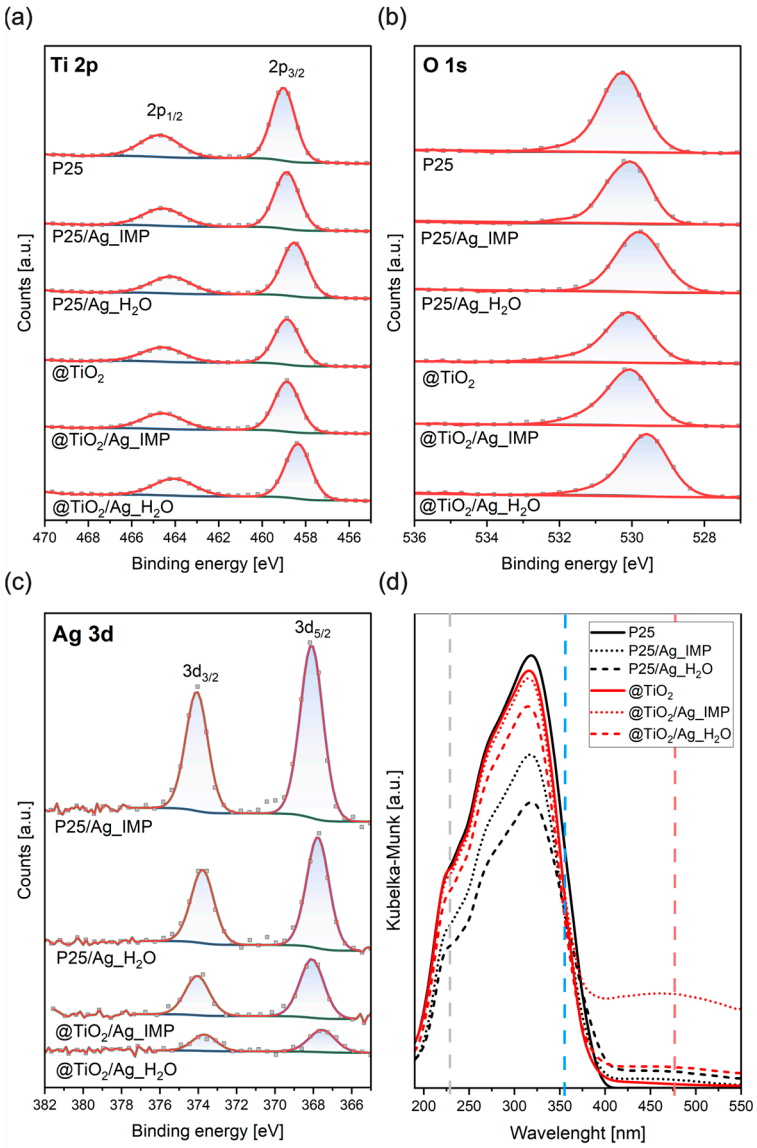

Figure 6. High resolution XPS spectra of Ti 2p (**a**), O 1s (**b**), Ag 3d (**c**) and UV-Vis-DR spectra in Kubelka–Munk function (**d**) for @TiO_2 and P25 materials before and after deposition of Ag using two different methods—IMP and H_2O.

Table 2. Positions of XPS Ti 2p, O 1s and Ag 3d peaks, surface Ag concentration and energy gap (Eg) for @TiO_2 and P25 materials before and after deposition of Ag using two different methods—IMP and H_2O.

Sample	Positions of XPS Peaks [eV]				Content of Surface Ag [at.%]	Eg [eV]
	Ti $2p_{3/2}$	Ti $2p_{1/2}$	Ag $3d_{5/2}$	Ag $3d_{3/2}$		
P25	459.0	464.7	-	-	-	3.20
P25/Ag_IMP	458.9	464.6	368.1	374.1	2.0	3.12
P25/Ag_H_2O	458.5	464.2	367.8	373.8	1.4	3.21
@TiO_2	458.9	464.6	-	-	-	3.27
@TiO_2/Ag_IMP	458.9	464.6	368.1	374.1	0.8	3.27
@TiO_2/Ag_H_2O	458.4	464.0	367.6	373.7	0.3	3.32

For each of the analyzed Ag-containing samples, a doublet of $3d_{5/2}$ and $3d_{3/2}$ characteristic of spin-orbit splitting in Ag atoms appears (Figure 6c) [56,57]. However, these peaks change their positions depending on the method used for the modification. The samples obtained by the IMP technique show the Ag $3d_{5/2}$ peak at 368.1 eV, while for the H_2O series, it is at 367.6–367.8 eV (Table 2). Based on these positions, it can be inferred about the dominant forms of Ag present on the surface, as photoelectron emission from metallic Ag^0 is usually observed at E_b = 368.2 eV [58], Ag_2O—E_b = 367.8 eV [59], and AgO—E_b = 367.4 eV [60]. The XPS Ag $3d_{5/2}$ peaks found in the studied materials suggest that, regardless of the type of support and the deposition method, Ag occurs as surface $Ag^{\delta+}$ species, where $0 < \delta < 1$ [55]. Nevertheless, the value of δ in the case of the samples obtained by the H_2O method is shifted towards +1 (Ag_2O form), while for the IMP materials towards 0 (Ag^0 species).

In order to further confirm the type of Ag species present on the TiO_2 supports (@TiO_2 and P25), UV-Vis-DR analysis was performed (Figure 6d). The bands originating from isolated Ag^+ ions occur at wavelengths of 190 and 220 nm [61]. Comparing the collected spectra for the starting and modified materials, no significant differences can be found in this range, which may, however, result from the strong absorption of TiO_2 [55]. In all modified materials, a broad band with a maximum at about 450 nm is observed. It is related to the presence of metallic Ag aggregates on the surface of the material [51,62].

Based on the UV-Vis-DR measurements, using the Tauc plot, the value of the energy gap (Eg) for the obtained materials was determined (Table 2). It can be noticed that the method of obtaining the TiO_2 support, and thus its phase composition, has a determining influence on Eg. In the case of a mixture of anatase and rutile phases (P25), the value of Eg (3.20 eV) is lower than for the @TiO_2 material (3.27 eV), in which anatase is accompanied only by a small admixture of rutile and brookite. It is worth noting, however, that the appearance of Ag species on the surface of @TiO_2 results in a further shift of Eg to a value as high as 3.32 eV.

Finally, the photocatalytic activity of the synthesized materials based on @TiO_2 and P25 were tested in the oxidation of 4NP using UV (Figure 7a) and Vis radiation source (Figure 7c). The results of fitting the first-order kinetics model (dashed lines) to the experimental points for all runs are shown in Figures 7b and 7d, respectively. It should be taken into account that low-power LED radiation sources (3.2 W and 8.2 W for UV and visible radiation, respectively) were used in this study. Such low energies forced the extension of the test duration to 6 h. In the case of UV radiation, the reference P25 material shows a much better efficiency in removing 4NP than @TiO_2. In addition, regardless of the support, the introduction of the additional Ag phase on the surface causes a significant deterioration in the efficiency of photocatalysts. Nevertheless, as shown by the determined kinetic parameters (Table 3), all materials accelerate the photodegradation of 4NP compared to the action of UV radiation in the absence of TiO_2 containing sample.

Table 3. Kinetic parameters of first kinetic order model determined for photocatalytic oxidation of 4NP using UV and Vis source on @TiO_2 and P25 materials before and after deposition of Ag using two different methods—IMP and H_2O.

Sample	UV (λ = 340 nm)			Vis (λ = 400–800 nm)		
	C/C_0	k [h^{-1}]	R^2	C/C_0	k [h^{-1}]	R^2
non (lamp)	0.696	0.052	0.9692	0.982	0.0028	0.9756
P25	0.004	1.8591	0.9988	0.973	0.0044	0.9952
P25/Ag_IMP	0.549	0.0913	0.9848	0.937	0.0096	0.9269
P25/Ag_H_2O	0.153	0.2992	0.9734	0.937	0.0072	0.7925
@TiO_2	0.297	0.1757	0.9718	0.896	0.0171	0.9895
@TiO_2/Ag_IMP	0.549	0.0913	0.9848	0.899	0.0182	0.9952
@TiO_2/Ag_H_2O	0.597	0.0715	0.9519	0.809	0.0376	0.9886

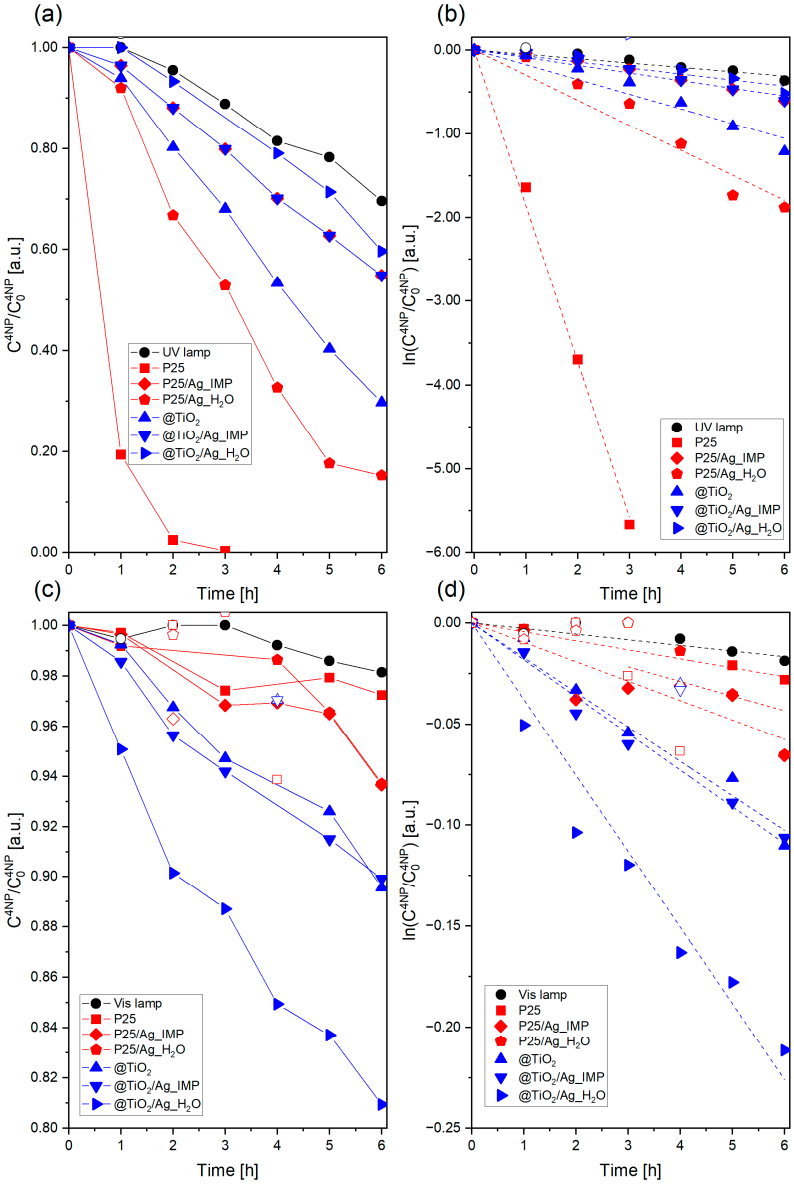

Figure 7. Results of photocatalytic oxidation of 4NP using UV radiation source (**a**) and Vis imitating source (**c**) with fitting first kinetic order model to experimental data (**b**,**d**) collected for @TiO_2 and P25 materials before and after deposition of Ag using two different methods—IMP and H_2O. Empty scatter points were excluded from linear fitting.

The observed degradation of the photocatalytic activity of the modified systems is most likely caused by high concentration of the Ag phase on the surface, which may result in the generation of recombination centers that quench the excited state of the photocatalyst [63,64]. In such a case the interaction between the radiation and the surface of material is also changed [64,65]. This effect is particularly evident for the P25 reference material. For the P25/Ag_IMP sample with a higher content of surface Ag than P25/Ag_H_2O (Table 2) the decrease in photoactivity is significant.

In the case of using a light source generating white light, the addition of the catalyst also accelerates the photodegradation of 4NP. It should be noted that the materials based on P25 are characterized by low photocatalytic activity in this radiation range. In addition, the P25 materials show similar efficiency regardless of the Ag deposition method. Improved photodegradation efficiency was observed in the case of using materials based on @TiO_2. The starting material shows almost 2 times higher efficiency in removing 4NP than commercial P25. What's more, it removes the pollutant much faster and more effectively

compared to the Ag-modified P25 materials. The increased efficiency may be related to the presence of the Ti^{3+} vacancy in the @TiO_2 structure [52]. In the case of the introduction of Ag by the IMP method, no significant improvement in the efficiency of the material was observed. Among all the tested materials, the @TiO_2/Ag_H_2O sample is the most effective. Almost 20% of the pollutant was removed in the presence of this photocatalyst during the 6 h irradiation period. Comparing to the system without the photocatalyst, a nearly 19-fold improvement was therefore obtained. Noticeable enhancement of photocatalytic properties after the Ag deposition is partly related to better charge separation in the electron-hole system [40]. This is because the electron ejected from the TiO_2 valence band is transferred to Ag^0 due to the lower Fermi level than the TiO_2 conduction band [63]. In this way, a Schottky barrier at metal(Ag^0)-semiconductor(TiO_2) is created, which influences the previously mentioned charge separation and increases recombination time of the electron-hole pair [66]. Therefore, Ag acts as an electron trap, being an electron donor for O_2 involved in the system [64].

The comparison to other studies using similar photocatalytic systems reveals high potential of the synthesized materials. Under artificial visible light (a 300 W radiation source) about 30% of 4NP was removed after 24 h of irritation [67]. The same efficiency of photodegradation was achieved in the presence of solar light irritation after 2 h [68]. However, it should be remembered that sunlight during a clear day carries an energy of ca. 1000 W/m^2. For this reason, it can be assumed that the developed @TiO_2/Ag_H_2O material should be much more effective than reported in the mentioned study [68].

3. Materials and Methods

3.1. Chemicals

Resorcinol (Avantor, Gliwice, Poland, >99.0%); melamine (Sigma-Aldrich, Schnelldrof, Germany, >99.0%); formaldehyde (Avantor, Gliwice, Poland, solution 36–38%); poly(vinyl alcohol) (PVA) (Avantor, Gliwice, Poland, M_W = 72,000, >99%); ethanol (Chempur, Piekary Śląskie, Poland, >98%); ammonia (Chempur, Piekary Śląskie, Poland, solution 25%); titanium(IV) butoxide (TBOT) (Sigma-Aldrich, Germany, >97%); isopropanol (Avantor, Gliwice, Poland, >99.0%); silver(I) nitrate (Avantor, Gliwice, Poland, > 99.0%); L-ascorbic acid (Stanlab, Lublin, Poland, >99.0%); sodium hydroxide (Chempur, Piekary Śląskie, Poland, >99.0%); 4-nitrophenol (4NP) (Acros Organics, Fair Lawn, NJ, USA, >99%); phosphate buffer pH = 7 (Supelco, Bellefonte, PA, USA); TiO_2 Aeroxide® (P25) (Evonik, Essen, Germany, p.a.); hydrogen peroxide (Avantor, Gliwice, Poland, 30%, p.a.); potassium bromide (Sigma Aldrich, Germany, spectral grade); nitrogen (Air Products, Świerzewo, Poland, grade 5.2).

3.2. Synthesis

3.2.1. Preparation of C@TiO_2 Composite

C@TiO_2 composite was produced using a spherical resin template (RMF), which was synthesized by polycondensation of resorcinol (5.0125 g), formaldehyde (7 mL) and melamine (1.3714 g) performed in a water-ethanol mixture (700 mL) at a volume ratio of 5:2. Poly(vinyl alcohol) (0.5059 g) was additionally introduced as a stabilizer, and the polycondensation process was initiated by an addition of an aqueous solution of ammonia (2.5 mL). The mixture was heated in an oil bath placed on a hot plate. The polycondensation was carried out with continuous stirring using a mechanical stirrer (200 rpm) at 40 °C for 24 h and then at 100 °C for 20 h. The mixture changed color from colorless to light brown and finally to brick red observed after aging at elevated temperature.

In the next step, the condensation process of amorphous TiO_2 was carried out on the synthesized RFM. For this purpose, 200 mL of the obtained suspension was introduced into a three-necked flask, equipped with a spiral condenser and placed on a magnetic stirrer. To the system maintained at 60 °C 63 mL of 7% TBOT solution in isopropanol was added dropwise under vigorous stirring. Subsequently, the temperature was raised to 100 °C and the mixture was left for the next 16 h. The suspension was then filtered on a Buchner funnel

and dried at 60 °C for 12 h. Finally, the material was carbonized in a tube furnace in a nitrogen flow (60 mL·min^{-1}) at 825 °C for 4 h with a constant rate of temperature increase (1 °C·min^{-1}). The resulting C@TiO_2 composite was removed from the furnace when the temperature dropped below 80 °C.

3.2.2. Deposition of Ag Nanoparticles

Silver nanoparticles were deposited in the amount of 1.0 mol% in relation to Ti in TiO_2 on two various supports (namely synthesized C@TiO_2 composite and reference material P25) using two methods: (i) impregnation (samples IMP) and (ii) deposition in distilled water in the presence of L-ascorbic acid (0.01 mol·L^{-1}) and sodium hydroxide (samples H_2O). An $AgNO_3$ solution (0.01 mol·L^{-1}) was selected as a source of Ag^+ ions. The impregnation method consisted in direct introduction of the aqueous $AgNO_3$ solution into the pores of the support, and then drying the impregnated material in a moisture analyzer. The deposition of Ag from the aqueous phase was carried out as follows. 0.2 g of NaOH was dissolved in 50 mL of distilled H_2O placed in a round bottom flask. Subsequently, 0.35 g of the support was added to the solution, followed by 2.1 mL of L-ascorbic acid and an appropriate amount of $AgNO_3$ solution. The suspension was sonicated for 30 min, and then the preparation was filtered and dried.

The prepared materials, including P25 series, were calcined in a tube furnace at 550 °C for 4 h under a constant nitrogen flow (60 mL·min^{-1}). The carbon core was removed from the starting and modified C@TiO_2 composites by thermal treatment in a muffle furnace using a two-stage temperature program: (i) 250 °C, 30 min, rate of heating = 7.6 °C·min^{-1}, followed by (ii) 500 °C, 6 h, rate of heating = 0.5 °C·min^{-1}. The resulting materials were denoted as @TiO_2, @TiO_2/Ag_H_2O and @TiO_2/Ag_IMP.

3.3. Characterization

Thermal analyses were done using a SDT Q600 thermobalance (TA Instruments). An amount of about 10 mg of a sample was introduced into a corundum crucible and heated under nitrogen atmosphere (total flow rate = 100 mL·min^{-1}) from 30 to 800 °C at a heating rate of 10 °C·min^{-1}.

Structure of the carbon samples was determined using powder X-ray diffraction (XRD). The XRD patterns were collected on a Bruker D2 Phaser instrument using Cu Kα radiation (λ = 1.54184 Å) and a LYNXEYE within a 2θ range of 5–80° (core-shell composites) or 20–80° (shell materials) at a step of 0.02°. TiO_2 phase content was determined according to Equation (1) [69]:

$$\%A = \frac{0.79 I_A}{I_R + 0.79 I_A} \cdot 100\% \quad (1)$$

where: I_A—intensity of anatase (101) diffraction line, I_R—intensity of rutile (110) diffraction line.

Textural properties of the materials were studied by low-temperature adsorption of nitrogen at −196 °C using a Micromeritics ASAP 2020 sorptometer. The adsorption measurement was preceded by an outgassing procedure at 250 °C for 6 h under vacuum.

Surface morphology of the samples was observed by an Apreo 2S LoVac scanning electron microscope (Thermo Fisher Scientific, Waltham, MA, USA). For imaging, the backscattered electron (BSE) mode was applied at an accelerating voltage of 10 kV and a beam current of 0.40 nA. The distribution of the investigated components was examined by an energy dispersive X-ray spectroscopy (EDX). The materials were mounted on a conductive carbon tape glued to pin-type SEM mounts and coated with gold (10 nm thick layer) using a Safematic CCU-010 HV vacuum sputter coater (Switzerland).

Particle size distribution was determined using dynamic light scattering measurements (DLS) in a Zetasizer Nano ZS analyzer (Malvern Instruments) working at 25 °C. The measurements were conducted in single use polystyrene cuvettes at 25 °C. The samples were diluted with distilled water and treated with ultrasounds for 30 min.

Surface analyses by X-ray photoelectron spectroscopy (XPS) were carried out in a system constructed by Prevac. The XPS spectra were collected using a monochromatized aluminum source AlKα (E = 1486.6 eV) and a hemispherical analyzer (VG SCIENTA R3000). Binding energy scale was calibrated by referring to a position of C 1s (E_b = 284.8 eV) typical of adventitious carbon. The Shirley background and fitting with the mixed function of Gauss and Lorentz (GL = 30) were used during interpretation of the spectra in the CasaXPS software.

UV-Vis-DR spectra were collected using an Evolution 220 spectrometer (Thermo Scientific) at wavelength range of 190–500 nm in the Kubelka–Munk function. Each sample was prepared as a smooth disc obtained by milling a sample (4 mg) with dry KBr (96 mg). The energy gap was determined by extrapolation of Tauc's plot [70].

3.4. Photocatalytic Activity

Photocatalytic tests in the oxidation of 4-nitrophenol (4NP) were carried out in a slurry reactor with constant air bubbling. The process was performed in phosphate buffer (pH = 7), selected as the reaction medium, at concentration of 4NP and a studied photocatalyst of 20 mg·L^{-1} and 0.8 g·L^{-1}, respectively. Before the test, the suspension was placed in an ultrasonic bath for 30 min to ensure homogenization of the photocatalyst. Before transferring the suspension to the reactor and adding 4NP, a 1 mL sample was taken and used as a background in spectrophotometric measurements. After placing the slurry in the reactor, air bubbling was started, 76.4 μL (0.58 mg) of 8 g·L^{-1} 4NP solution was added and left in the dark for 30 min to equilibrate the system. Then, 24.6 μL of 30% H_2O_2 was introduced. After 3 min, a "zero" sample was taken, on the basis of which the initial concentration of 4NP in the reaction mixture was determined. The irradiation time (ThorLabs, M340L4, λ = 340 nm—UV source; ThorLabs, MWWHLP, λ = 400–800 nm—Vis source) was 6 h. Changes in the 4NP concentration after 30, 60, 120, 180, 240, 300 and 360 min were examined by UV–Vis measurements in an Evolution 220 spectrophotometer (Thermo Scientific) equipped with a xenon lamp. The spectra were collected in the wavelength range of 200–750 nm with resolution of 1 nm. The measurements were made using a quartz microcuvette (ThorLabs) for samples after separating suspended photocatalyst with a syringe filter (Chemland, Stargard, Poland, PTFE disc, 0.44 μm).

4. Conclusions

The above discussion confirmed that it is possible to form the structure of C@TiO_2 core-shell composites using the bottom-up synthesis strategy, and the photocatalytic properties of the oxide shell can be used in degradation of phenolic compounds in aqueous solutions. Particular emphasis should be placed on changing the properties of the studied TiO_2 materials by the deposition of Ag nanoparticles. Two modification paths were compared, consisting of impregnation on the one hand, and precipitation of the silver phase on the other, using either the C@TiO_2 composite or the P25 reference material as the modified objects. Different dispersion of Ag nanoparticles was obtained, and thus their surface concentration and contact between Ag^0 and TiO_2 support, and consequently different energy gap values. Finally, a significant increase in the photocatalytic activity of TiO_2 shells derived from the C@TiO_2 composite materials was observed in the degradation of 4-nitrophenol in the visible light range. Thus, the role of Ag particles as an electron trap activating electron transfer during the oxidation of organic pollutant was revealed. From this point of view, the developed materials promise very well to be used in systems intended for combined adsorption-photocatalytic elimination of phenolic pollutants.

Author Contributions: Conceptualization, K.S. and P.K.; methodology, K.S. and P.K.; investigation, K.S., R.L., A.R., T.B. and M.D.; writing—original draft preparation, K.S. and P.K.; writing—review and editing, K.S. and P.K.; visualization, K.S., A.R. and M.D.; supervision, P.K. All authors have read and agreed to the published version of the manuscript.

Funding: K.S. has been partly supported by the EU Project POWR.03.02.00-00-I004/16. Some measurements were carried out with the equipment purchased thanks to the financial support of the European Regional Development Fund in the framework of the Polish Innovation Economy Operational Program (contract no. POIG.02.01.00-12-023/08). The research has been supported by a grant from the Faculty of Chemistry under the Strategic Programme Excellence Initiative at Jagiellonian University.

Data Availability Statement: The data presented in this study are available on request from the corresponding author.

Conflicts of Interest: The authors declare no conflict of interest. The funders had no role in the design of the study; in the collection, analyses, or interpretation of data; in the writing of the manuscript, or in the decision to publish the results.

References

1. Jurado, A.; Vàzquez-Suñé, E.; Carrera, J.; de Alda, M.L.; Pujades, E.; Barceló, D. Emerging organic contaminants in groundwater in Spain: A review of sources, recent occurrence and fate in a European context. *Sci. Total. Environ.* **2012**, *440*, 82–94. [CrossRef] [PubMed]
2. Jurado, A.; Pujades, E.; Walther, M.; Diaz-Cruz, M.S. Occurrence, fate, and risk of the organic pollutants of the surface water watch List in European groundwaters: A review. *Environ. Chem. Lett.* **2022**, *20*, 3313–3333. [CrossRef]
3. Diao, P.; Chen, Q.; Wang, R.; Sun, D.; Cai, Z.; Wu, H.; Duan, S. Phenolic endocrine-disrupting compounds in the Pearl River Estuary: Occurrence, bioaccumulation and risk assessment. *Sci. Total. Environ.* **2017**, *584–585*, 1100–1107. [CrossRef] [PubMed]
4. Youbin, S.; Yongde, Y.; Zaipeng, W.; Ruyi, W.; Dapeng, D. Bioaccumulation and Biodegration of Phenol by the Algae Micro-cystis aeruginosa Kutz. *J. Anhui Agric. Univ.* **2000**, *27*, 269–271.
5. Anku, W.W.; Mamo, M.A.; Govender, P.P. Chapter 17. Phenolic Compounds in Water: Sources, Reactivity, Toxicity and Treatment Methods. In *Phenolic Compounds—Natural Sources, Importance and Applications*, 1st ed.; Soto-Hernández, M., Palma-Tenango, M., García-Mateos, R., Eds.; IntechOpen: Rijeka, Croatia, 2017; Volume 1, pp. 419–443.
6. Mahugo-Santana, C.; Sosa-Ferrera, Z.; Torres-Padrón, M.E.; Santana-Rodríguez, J.J. Analytical Methodologies for the Determination of Nitroimidazole Residues in Biological and Environmental Liquid Samples: A Review. *Anal. Chim. Acta* **2010**, *665*, 113–122. [CrossRef]
7. Hättenschwiler, S.; Vitousek, R.M. The Role of Polyphenols in Terrestrial Ecosystem Nutrient Cycling. *Trends Ecol. Evol.* **2000**, *15*, 238–243. [CrossRef]
8. Mukherjee, S.; Basak, B.; Bhunia, B.; Dey, A.; Mondal, B. Potential use of polyphenol oxidases (PPO) in the bioremediation of phenolic contaminants containing industrial wastewater. *Rev. Environ. Sci. Bio/Technol.* **2013**, *12*, 61–73. [CrossRef]
9. Raza, W.; Lee, J.; Raza, N.; Luo, Y.; Kim, K.-H.; Yang, J. Removal of phenolic compounds from industrial waste water based on membrane-based technologies. *J. Ind. Eng. Chem.* **2019**, *71*, 1–18. [CrossRef]
10. Dąbrowski, A.; Podkościelny, P.; Hubicki, Z.; Barczak, M. Adsorption of phenolic compounds by activated carbon—A critical review. *Chemosphere* **2005**, *58*, 1049–1070. [CrossRef]
11. Mohammadi, S.; Kargari, A.; Sanaeepur, H.; Abbassian, K.; Najafi, A.; Mofarrah, E. Phenol removal from industrial wastewaters: A short review. *Desalin. Water Treat.* **2013**, *53*, 2215–2234. [CrossRef]
12. Said, K.A.M.; Ismail, A.F.; Karim, Z.A.; Abdullah, M.S.; Hafeez, A. A review of technologies for the phenolic compounds recovery and phenol removal from wastewater. *Process. Saf. Environ. Prot.* **2021**, *151*, 257–289. [CrossRef]
13. Ng, Y.S.; Jayakumar, N.S.; Hashim, M.A. Performance Evaluation of Organic Emulsion Liquid Membrane on Phenol Removal. *J. Hazard. Mater.* **2010**, *184*, 255–260. [CrossRef]
14. Pradeep, N.V.; Anupama, S.; Navya, K.; Shalini, H.N.; Idris, M.; Hampannavar, U.S. Biological removal of phenol from wastewaters: A mini review. *Appl. Water Sci.* **2014**, *5*, 105–112. [CrossRef]
15. Mojoudi, N.; Mirghaffari, N.; Soleimani, M.; Shariatmadari, H.; Belver, C.; Bedia, J. Phenol adsorption on high microporous activated carbons prepared from oily sludge: Equilibrium, kinetic and thermodynamic studies. *Sci. Rep.* **2019**, *9*, 19352. [CrossRef]
16. Ren, T.; Jin, Z.; Yang, J.; Hu, R.; Zhao, F.; Gao, X.; Zhao, C. Highly Efficient and Stable p-$LaFeO_3$/n-ZnO Heterojunction Photocatalyst for Phenol Degradation under Visible Light Irradiation. *J. Hazard. Mater.* **2019**, *377*, 195–205. [CrossRef]
17. Busca, G.; Berardinelli, S.; Resini, C.; Arrighi, L. Technologies for the removal of phenol from fluid streams: A short review of recent developments. *J. Hazard. Mater.* **2008**, *160*, 265–288. [CrossRef]
18. Makatsa, T.J.; Baloyi, J.; Ntho, T.; Masuku, C.M. Catalytic wet air oxidation of phenol: Review of the reaction mechanism, kinetics, and CFD modeling. *Crit. Rev. Environ. Sci. Technol.* **2020**, *51*, 1891–1923. [CrossRef]
19. Besson, M.; Descorme, C.; Bernardi, M.; Gallezot, P.; Di Gregorio, F.; Grosjean, N.; Minh, D.P.; Pintar, A. Supported noble metal catalysts in the catalytic wet air oxidation of industrial wastewaters and sewage sludges. *Environ. Technol.* **2010**, *31*, 1441–1447. [CrossRef]
20. De-Bin, L.; Duo, W.; Zi-Sheng, J. Catalytic Wet Air Oxidation of Sewage Sludge: A Review. *Curr. Organocatal.* **2020**, *7*, 199–211.
21. Li, X.; Cubbage, J.W.; Tetzlaff, T.A.; Jenks, W.S. Photocatalytic Degradation of 4-Chlorophenol. 1. The Hydroquinone Pathway. *J. Org. Chem.* **1999**, *64*, 8509–8524. [CrossRef]

22. Chen, D.; Ray, A.K. Photodegradation kinetics of 4-nitrophenol in TiO_2 suspension. *Water Res.* **1998**, *32*, 3223–3234. [CrossRef]
23. Subramaniam, M.N.; Goh, P.S.; Lau, W.J.; Ng, B.C.; Ismail, A.F. Chapter 3—Development of Nanomaterial-Based Photocatalytic Membrane for Organic Pollutants Removal. In *Advanced Nanomaterials for Membrane Synthesis and its Applications*, 1st ed.; Lau, W.J., Ismail, A.F., Isloor, A., Al-Ahmed, A., Eds.; Elsevier: Amsterdam, The Netherlands, 2019; Volume 1, pp. 45–67.
24. Vaiano, V.; Matarangolo, M.; Murcia, J.; Rojas, H.; Navío, J.; Hidalgo, M. Enhanced photocatalytic removal of phenol from aqueous solutions using ZnO modified with Ag. *Appl. Catal. B Environ.* **2018**, *225*, 197–206. [CrossRef]
25. Davis, A.P.; Huang, C.P. Removal of Phenols from Water by a Photocatalytic Oxidation Process. *Water Sci. Technol.* **1989**, *21*, 455–464. [CrossRef]
26. Al-Hamdi, A.M.; Rinner, U.; Sillanpää, M. Tin Dioxide as a Photocatalyst for Water Treatment: A Review. *Process Saf. Environ. Prot.* **2017**, *107*, 190–205. [CrossRef]
27. Mele, G.; Słota, R.; Dyrda, G. Chapter 12—Semiconductor @ Sensitizer Composites for Enhanced Photoinduced Processes. In *Materials Science in Photocatalysis*, 1st ed.; Garcia Lopez, E., Palmisano, L., Eds.; Elsevier: Amsterdam, The Netherlands, 2021; Volume 1, pp. 183–209.
28. Dou, L.; Zhong, J.; Li, J.; Luo, J.; Zeng, Y. Fabrication of Bi_2SiO_5 hierarchical microspheres with an efficient photocatalytic performance for rhodamine B and phenol removal. *Mater. Res. Bull.* **2019**, *116*, 50–58. [CrossRef]
29. Völz, H.G. Pigments, Inorganic. In *Ullmann's Encyclopedia of Industrial Chemistry*, 6th ed.; Ley, C., Elvers, B., Eds.; Wiley-VCH: Weinheim, Germany, 2002; Volume: Dyes and Pigments, pp. 1–145.
30. Shawabkeh, R.A.; Khashman, O.A.; Bisharat, G.I. Photocatalytic Degradation of Phenol Using Fe-TiO_2 by Different Illumination Sources. *Int. J. Chem.* **2010**, *2*, 10–18. [CrossRef]
31. Hanaor, D.A.H.; Sorrell, C.C. Review of the Anatase to Rutile Phase Transformation. *J. Mater. Sci.* **2011**, *46*, 855–874. [CrossRef]
32. Basavarajappa, P.S.; Patil, S.B.; Ganganagappa, N.; Reddy, K.R.; Raghu, A.V.; Reddy, C.V. Recent progress in metal-doped TiO_2, non-metal doped/codoped TiO_2 and TiO_2 nanostructured hybrids for enhanced photocatalysis. *Int. J. Hydrog. Energy* **2019**, *45*, 7764–7778. [CrossRef]
33. Mani, A.; Reddy, P.K.; Srinivaas, M.; Ghosal, P.; Xanthopoulos, N.; Subrahmanyam, C. Facile synthesis of efficient visible active C-doped TiO_2 nanomaterials with high surface area for the simultaneous removal of phenol and Cr(VI). *Mater. Res. Bull.* **2015**, *61*, 391–399. [CrossRef]
34. Huang, W.C.; Ting, J.-M. Novel nitrogen-doped anatase TiO_2 mesoporous bead photocatalysts for enhanced visible light response. *Ceram. Int.* **2017**, *43*, 9992–9997. [CrossRef]
35. Quesada-Cabrera, R.; Sotelo-Vázquez, C.; Quesada-González, M.; Melián, E.P.; Chadwick, N.; Parkin, I.P. On the apparent visible-light and enhanced UV-light photocatalytic activity of nitrogen-doped TiO_2 thin films. *J. Photochem. Photobiol. A Chem.* **2017**, *333*, 49–55. [CrossRef]
36. Belekbir, S.; El Azzouzi, M.; El Hamidi, A.; Rodríguez-Lorenzo, L.; Santaballa, J.A.; Canle, M. Improved Photocatalyzed Degradation of Phenol, as a Model Pollutant, over Metal-Impregnated Nanosized TiO_2. *Nanomaterials* **2020**, *10*, 996. [CrossRef]
37. Dobrosz-Gómez, I.; Gómez-García, M.; Zamora, S.L.; GilPavas, E.; Bojarska, J.; Kozanecki, M.; Rynkowski, J. Transition metal loaded TiO_2 for phenol photo-degradation. *Comptes Rendus Chim.* **2015**, *18*, 1170–1182. [CrossRef]
38. Ayati, A.; Ahmadpour, A.; Bamoharram, F.F.; Tanhaei, B.; Mänttäri, M.; Sillanpää, M. A Review on Catalytic Applications of Au/TiO_2 Nanoparticles in the Removal of Water Pollutant. *Chemosphere* **2014**, *107*, 163–174. [CrossRef]
39. Espino-Estévez, M.R.; Fernández-Rodríguez, C.; González-Díaz, O.M.; Araña, J.; Espinós, J.P.; Ortega-Méndez, J.A.; Doña-Rodríguez, J.M. Effect of TiO_2–Pd and TiO_2–Ag on the Photocatalytic Oxidation of Diclofenac, Isoproturon and Phenol. *Chem. Eng. J.* **2016**, *298*, 82–95. [CrossRef]
40. Scott, T.; Zhao, H.; Deng, W.; Feng, X.; Li, Y. Photocatalytic degradation of phenol in water under simulated sunlight by an ultrathin MgO coated Ag/TiO2 nanocomposite. *Chemosphere* **2018**, *216*, 1–8. [CrossRef]
41. Alberici, R.M.; Jardim, W.F. Photocatalytic Degradation of Phenol and Chlorinated Phenols Using Ag@TiO_2 in a Slurry Reactor. *Wat. Res.* **1994**, *28*, 1845–1849. [CrossRef]
42. UK Disagree with EU Position on Titanium Dioxide, Food Safety News. 9 March 2022. Available online: https://www.foodsafetynews.com/2022/03/uk-disagrees-with-eu-position-on-titanium-dioxide (accessed on 20 February 2023).
43. Luo, Z.; Li, Z.; Xie, Z.; Sokolova, I.M.; Song, L.; Peijnenburg, W.J.G.M.; Hu, M.; Wang, Y. Rethinking Nano-TiO_2 Safety: Overview of Toxic Effects in Humans and Aquatic Animals. *Small* **2020**, *16*, 2002019. [CrossRef]
44. Jiang, X.; Manawan, M.; Feng, T.; Qian, R.; Zhao, T.; Zhou, G.; Kong, F.; Wang, Q.; Dai, S.; Pan, J.-H. Anatase and Rutile in Evonik Aeroxide P25: Heterojunctioned or Individual Nanoparticles? *Catalysts* **2018**, *300*, 12–17. [CrossRef]
45. Sidor, K.; Berniak, T.; Łątka, P.; Rokicińska, A.; Michalik, M.; Kuśtrowski, P. Tailoring Properties of Resol Resin-Derived Spherical Carbons for Adsorption of Phenol from Aqueous Solution. *Molecules* **2021**, *26*, 1736. [CrossRef]
46. Zhao, Y.; Wang, S.; Shen, Y.; Lu, X. Effects of Nano-TiO_2 on Combustion and Desulfurization. *Energy* **2013**, *56*, 25–30. [CrossRef]
47. Li, W.-X.; Stampfl, C.; Scheffler, M. Oxygen adsorption on Ag(111): A density-functional theory investigation. *Phys. Rev. B* **2002**, *65*, 075407. [CrossRef]
48. Lekshmi, G.S.; Ramasamy, T.; Bazaka, O.; Levchenko, I.; Bazaka, K.; Govindan, R.; Mandhakini, M. Antioxidant, Anti-Bacterial, and Congo Red Dye Degradation Activity of AgxO-Decorated Mustard Oil-Derived rGO Nanocomposites. *Molecules* **2022**, *27*, 5950. [CrossRef] [PubMed]

49. Van Noi, N.; Cam, B.D.; Cam, N.T.D.; Dong, P.T.; Phuong, D.T. Silver Doped Titania Materials on Clay Support for Enhanced Visible Light Photocatalysis. *e-J. Surf. Sci. Nanotechnol.* **2011**, *9*, 454–457. [CrossRef]
50. Lazzarini, A.; Piovano, A.; Pellegrini, R.; Agostini, G.; Rudić, S.; Lamberti, C.; Groppo, E. Graphitization of Activated Carbon: A Molecular-Level Investigation by INS, DRIFT, XRD and Raman Techniques. *Phys. Procedia* **2016**, *85*, 20–26. [CrossRef]
51. Xu, H.; Li, G.; Liu, N.; Zhu, K.; Zhu, G.; Jin, S. Ag@Hierarchical TiO_2 Core-Shell Nanostructures for Enhanced Photocatalysis. *Mater. Latt.* **2015**, *142*, 324–327. [CrossRef]
52. Xu, Y.; Wu, S.; Wan, P.; Sun, J.; Hood, Z.D. Introducing Ti^{3+} defect based on lattice distortion for enhanced visible light photoreactivuty in TiO_2 microspheres. *RSC Adv.* **2017**, *7*, 3261–32467.
53. Göpel, W.; Anderson, J.; Frankel, D.; Jaehnig, M.; Phillips, K.; Schäfer, J.; Rocker, G. Surface defects of TiO_2(110): A combined XPS, XAES AND ELS study. *Surf. Sci.* **1984**, *139*, 333–346. [CrossRef]
54. Akel, S.; Dillert, R.; Balayeva, N.O.; Boughaled, R.; Koch, J.; El Azzouzi, M.; Bahnemann, D.W. Ag/Ag_2O as a Co-Catalyst in TiO_2 Photocatalysis: Effect of the Co-Catalyst/Photocatalyst Mass Ratio. *Catalysts* **2018**, *8*, 647. [CrossRef]
55. Fang, R.; He, M.; Huang, H.; Feng, Q.; Ji, J.; Zhan, Y.; Leung, D.Y.; Zhao, W. Effect of redox state of Ag on indoor formaldehyde degradation over Ag/TiO_2 catalyst at room temperature. *Chemosphere* **2018**, *213*, 235–243. [CrossRef]
56. Lin, X.; Rong, F.; Fu, D.; Yuan, C. Enhanced photocatalytic activity of fluorine doped TiO_2 by loaded with Ag for degradation of organic pollutants. *Powder Technol.* **2012**, *219*, 173–178. [CrossRef]
57. Yang, X.; Wang, Y.; Xu, L.; Yu, X.; Guo, Y. Silver and Indium Oxide Codoped TiO_2 Nanocomposites with Enhanced Photo-catalytic Activity. *J. Phys. Chem. C* **2008**, *112*, 11481–11489. [CrossRef]
58. Zhang, H.; Wang, G.; Lv, X.; Li, J. Tuning Photoelectrochemical Performances of Ag-TiO_2 Nanocomposites via Reduction/Oxidation of Ag. *Chem. Mater.* **2008**, *20*, 6543–6549. [CrossRef]
59. Grünert, W.; Brückner, A.; Hofmeister, H.; Claus, P. Structural Properties of Ag/TiO_2 Catalysts for Acrolein Hydrogenation. *J. Phys. Chem. B* **2004**, *108*, 5709–5717. [CrossRef]
60. Lai, Y.; Chen, Y.; Zhuang, H.; Lin, C. A facile method for synthesis of Ag/TiO_2 nanostructures. *Mater. Lett.* **2008**, *62*, 3688–3690. [CrossRef]
61. Keshavaraja, A.; She, X.; Flytzani-Stephanopoulos, M. Selective catalytic reduction of NO with methane over Ag-alumina catalysts. *Appl. Catal. B Environ.* **2000**, *27*, L1–L9. [CrossRef]
62. Kundakovic, L.; Flytzani-Stephanopoulos, M. Deep oxidation of methane over zirconia supported Ag catalysts. *Appl. Catal. A Gen.* **1999**, *183*, 35–51. [CrossRef]
63. Sung-Suh, H.M.; Choi, J.R.; Hah, H.J.; Koo, S.M.; Bae, Y.C. Comparison of Ag deposition effects on the photocatalytic activity of nanoparticulate TiO_2 under visible and UV light irradiation. *J. Photochem. Photobiol. A Chem.* **2004**, *163*, 37–44. [CrossRef]
64. Jaafar, N.; Jalil, A.; Triwahyono, S.; Efendi, J.; Mukti, R.; Jusoh, R.; Jusoh, N.; Karim, A.; Salleh, N.; Suendo, V. Direct in situ activation of Ag0 nanoparticles in synthesis of Ag/TiO_2 and its photoactivity. *Appl. Surf. Sci.* **2015**, *338*, 75–84. [CrossRef]
65. Harifi, T.; Montazer, M. Fe^{3+}: Ag/TiO_2 Nanocomposite: Synthesis, Characterization and Photocatalytic Activity under UV and Visible Light Irritation. *Appl. Catal. A Gen.* **2014**, *473*, 104–115. [CrossRef]
66. Zielińska, A.; Kowalska, E.; Sobczak, J.W.; Łącka, I.; Gazda, M.; Ohtani, B.; Hupka, J.; Zaleska, A. Silver-doped TiO_2 prepared by microemulsion method: Surface properties, bio- and photoactivity. *Sep. Purif. Technol.* **2010**, *72*, 309–318. [CrossRef]
67. Mahy, J.G.; Lambert, S.D.; Léonard, G.L.-M.; Zubiaur, A.; Olu, P.-Y.; Mahmoud, A.; Boschini, F.; Heinrichs, B. Towards a large scale aqueous sol-gel synthesis of doped TiO_2: Study of various metallic dopings for the photocatalytic degradation of pnitrophenol. *J. Photochem. Photobiol. A* **2016**, *329*, 189–202. [CrossRef]
68. Hamrouni, A.; Azzouzi, H.; Rayes, A.; Palmisano, L.; Ceccato, R.; Parrino, F. Enhanced Solar Light Photocatalytic Activity of Ag Doped TiO_2–Ag_3PO_4 Composites. *Nanomaterials* **2020**, *10*, 795. [CrossRef] [PubMed]
69. Thompson, T.L.; Yates, J.T. Surface Science Studies of the Photoactivation of TiO_2 New Photochemical Processes. *Chem. Rev.* **2006**, *106*, 4428–4453. [CrossRef] [PubMed]
70. Makuła, P.; Pacia, M.; Macyk, W. How To Correctly Determine the Band Gap Energy of Modified Semiconductor Photocatalysts Based on UV–Vis Spectra. *J. Phys. Chem. Lett.* **2018**, *9*, 6814–6817. [CrossRef]